NEOPLASIA
www.neoplasia.com

Volume 14 Number 3 March 2012 pp. 169–177 169

Imaging Therapeutic PARP Inhibition *In Vivo* through Bioorthogonally Developed Companion Imaging Agents[1,2]

Thomas Reiner*,[3], Jessica Lacy*,[3], Edmund J. Keliher*,[3], Katherine S. Yang*, Adeeti Ullal*, Rainer H. Kohler*, Claudio Vinegoni* and Ralph Weissleder*,†

*Center for Systems Biology, Massachusetts General Hospital, Boston, MA, USA; †Department of Systems Biology, Harvard Medical School, Boston, MA, USA

Abstract

A number of small-molecule poly (ADP-ribose) polymerase (PARP) inhibitors are currently undergoing advanced clinical trials. Determining the distribution and target inhibitory activity of these drugs in individual subjects, however, has proven problematic. Here, we used a PARP agent for positron emission tomography–computed tomography (PET-CT) imaging (^{18}F-BO), which we developed based on the Olaparib scaffold using rapid bioorthogonal conjugation chemistries. We show that the bioorthogonal ^{18}F modification of the parent molecule is simple, highly efficient, and well tolerated, resulting in a half maximal inhibitory concentration (IC_{50}) of 17.9 ± 1.1 nM. Intravital imaging showed ubiquitous distribution of the drug and uptake into cancer cells, with ultimate localization within the nucleus, all of which were inhibitable. Whole-body PET-CT imaging showed tumoral uptake of the drug, which decreased significantly, after a daily dose of Olaparib. Standard ^{18}F-fludeoxyglucose imaging, however, failed to detect such therapy-induced changes. This research represents a step toward developing a more generic approach for the rapid codevelopment of companion imaging agents based on small-molecule therapeutic inhibitors.

Neoplasia (2012) 14, 169–177

Introduction

DNA breaks occur naturally during the course of each cell cycle. In order for a cell to survive, however, these defects must be repaired. Poly (ADP-ribose) polymerase (PARP) and breast cancer susceptibility proteins (BRCA) are two proteins that have specific roles in repairing such breaks, namely PARP repairs single-strand breaks and BRCA repairs double-strand breaks. In cases where BRCA is mutated (i.e., not functional), PARP is able to repair both types of DNA breaks, and thus, these cells depend solely on the PARP repair mechanism. Small-molecule PARP inhibitors have received significant attention when combined with DNA-damaging agents in BRCA-negative tumors (synthetic lethality) [1]. Yet, despite the compelling scientific rationale for the use of these agents as well as encouragement from early clinical trials [1–3], more recent trials in triple-negative breast cancers [4] and in ovarian cancer [5] have resulted in disappointment. One issue in these studies has been the lack of clearly defined molecular biomarkers of efficacy. Indeed, recent trials have been heavily reliant on indirect measures of cancer regression derived from RECIST (Response Evaluation Criteria In Solid Tumors), tumor volumetrics or plasma biomarker methods (CA125, circulating cancer cells). These approaches could be considerably enhanced by the performance of tandem measurements of drug distribution (pharmacokinetics) as well as direct measurements of drug effects (pharmacodynamics) on their intended target.

Using newer bioorthogonal approaches, a number of platform technologies have been recently introduced, which facilitate rapid labeling of small-molecule drugs with ^{18}F for rapid proof-of-principle preclinical

Address all correspondence to: Ralph Weissleder, MD, PhD, Center for Systems Biology, Massachusetts General Hospital, 185 Cambridge St, CPZN 5206, Boston, MA 02114. E-mail: rweissleder@mgh.harvard.edu

[1]This study was funded in part by National Institutes of Health grants R01EB010011 and P50CA86355 (R.W.). K.S. Yang was supported by a National Institutes of Health grant T32-CA79443, and T. Reiner was supported by a grant from the German Academy of Sciences Leopoldina (LPDS 2009-24). The authors have no conflicts of interest to declare. The costs of publication of this article were defrayed, in part, by the payment of page charges. This article must therefore be hereby-marked *advertisement* in accordance with 18 U.S.C. Section 1734 solely to indicate this fact.

[2]This article refers to supplementary materials, which are designated by Figures W1 to W3 and are available online at www.neoplasia.com.

[3]These authors contributed equally for this study.

Received 22 February 2012; Revised 22 February 2012; Accepted 27 February 2012

 1522-8002/12/$25.00
DOI 10.1593/neo.12414

imaging [6]. Although it is synthetically feasible to produce ^{18}F-labeled small-molecule PARP inhibitors, how these agents might behave in different cancers, particularly ovarian and pancreatic cancers, has remained unclear. In the current study, we thus performed a more systematic preclinical approach involving biologic validation studies in murine models and using a prototype ^{18}F radioactive and a fluorescent PARP inhibitor platform based on the Olaparib (AZD2281) scaffold. The ^{18}F bioorthogonally (BO)–labeled Olaparib (^{18}F-BO) [6] and the fluorescent analog (FL-BO) were then tested in mouse models of ovarian and pancreatic cancer. We hypothesized that use of these BO agents would allow quantitation of PARP expression levels *in vivo*. To test this hypothesis, we designed a series of experiments that address the following questions: 1) What is the imaging profile of ^{18}F-BO in cancer models? 2) Do imaging signals from these agents correlate with PARP expression levels *in vivo*? 3) Do the imaging agents colocalize with PARP inside cancer cells? 4) How does ^{18}F-BO imaging compare to ^{18}F-FDG positron emission tomography (PET) imaging? Here, we show that ^{18}F-BO represents a highly selective agent for imaging PARP *in vivo*. Furthermore, ^{18}F-BO allows accurate prediction of target inhibition (superior to PET FDG imaging), and it has been found to accumulate inside the nucleus of tumor cells. We anticipate that this class of agent will be beneficial to current clinical trials not only by enabling direct measures of target occupancy but also for establishing drug doses based on biologic rather than toxicity grounds and for identifying treatment failures.

Materials and Methods

Unless otherwise noted, all reagents were purchased from Sigma-Aldrich (St. Louis, MO) and used without further purification. BODIPY FL succinimidyl ester was purchased from Invitrogen (Carlsbad, CA). Olaparib (AZD2281) was purchased from Selleck Chemicals (Houston, TX). 4-[[4-Fluoro-3-(piperazine-1-carbonyl)phenyl]methyl]-2*H*-phthalazin-1-one, AZD2281-Tz, ^{18}F-TCO, and ^{18}F-BO were synthesized as described elsewhere [6–8]. [^{18}F]-Fluoride (n.c.a.) and ^{18}F-fludeoxyglucose (^{18}F-FDG) were purchased from PETNET Solutions (Woburn, MA). High performance liquid chromatography electrospray ionization mass spectrometry (HPLC-ESI-MS) and high-performance liquid chromatography (HPLC) purifications were performed on a Waters (Milford, MA) LC-MS system. For LC-ESI-MS analyses, a Waters XTerra C18 5 μm column was used. For preparative runs, an Atlantis Prep T3 OBD 5-μm column was used. High-resolution ESI mass spectra were obtained on a Bruker Daltonics APEXIV 4.7-T Fourier transform mass spectrometer (FT-ICR-MS) in the Department of Chemistry Instrumentation Facility at the Massachusetts Institute of Technology. Proton nuclear magnetic resonance (^{1}H nuclear magnetic resonance [NMR]) spectra were recorded on a Varian AS-400 (400 MHz) spectrometer. Chemical shifts for protons are reported in parts per million (ppm) and are referenced against the dimethylsulfoxide lock signal (^{1}H, 2.50 ppm). Data are reported as follows: chemical shift, multiplicity (s = singlet, d = doublet, t = triplet, m = multiplet), coupling constants (Hz), and integration.

Synthesis of FL-BO

A solution of BODIPY FL succinimidyl ester (5.0 mg, 12.8 μmol) in acetonitrile (250 μl) was added to a solution of 4-[[4-fluoro-3-(piperazine-1-carbonyl)phenyl]methyl]-2*H*-phthalazin-1-one (4.7 mg, 12.8 μmol) and triethylamine (4.6 μl, 64.2 μmol) in acetonitrile (250 μl). The reaction mixture was stirred for 4 hours at room temperature and purified through HPLC to yield the title compound as an orange solid (5.7 mg, 8.9 μmol, 70%). ^{1}H NMR (400 MHz, DMSO-d_6) δ = 12.59 (s, 1H), 8.26 (d, $^3J_{HH}$ = 7.6, 1H), 7.96 (d, $^3J_{HH}$ = 7.8, 1H), 7.92-7.80 (m, 2H), 7.69 (s, 1H), 7.47-7.41 (m, 1H), 7.39-7.34 (m, 1H), 7.23 (t, $^3J_{HH}$ = 9.0, 1H), 7.09 (s, 1H), 6.45-6.38 (m, 1H), 6.30 (s, 1H), 4.33 (s, 2H), 3.66-3.05 (m, 10H), 2.80-2.68 (m, 2H), 2.48-2.44 (m, 3H), 2.26 (s, 3H); ^{19}F NMR (376 MHz, DMSO-d_6) δ = -119.4 (s, 1F), -142.8 (q, J_{BF} = 33 Hz, 2F); LC-ESI-MS(+) *m/z* = 621.4 [M – F]$^+$, 641.4 [M + H]$^+$, 663.4 [M + H]$^+$; LC-ESI-MS(–) *m/z* = 619.3 [M – 2H – F]$^-$, 639.3 [M – H]$^-$; HRMS-ESI [M – H]$^+$ *m/z* calculated for [$C_{32}H_{33}BF3N_6O_3$]$^+$ 641.2671, found 641.2688 [M + H]$^+$.

PARP-1 IC_{50} Determination

A commercially available colorimetric assay (Trevigen, Gaithersburg, MD) was used to measure PARP-1 activity *in vitro* in the presence of varying concentrations of FL-BO. Three-fold dilutions of FL-BO (final concentrations ranging from 3.3 μM to 0.1 nM) were incubated with 0.5 U of PARP high specific activity (HSA) enzyme for 10 minutes in histone-coated 96-well plates. All experiments were carried out in triplicate. Positive control samples did not contain inhibitor, and background measurement samples did not contain PARP-1. All reaction mixtures were adjusted to a final volume of 50 μl and a final concentration of 2% dimethyl sulfoxide (DMSO) in assay buffer. The remainder of the assay was performed according to the manufacturer's instructions. PARP-1 activity was measured by absorbance at 450 nm in each well using a Tecan Safire^2 microplate reader (Tecan Group, Mannedorf, Switzerland).

Cancer Cell Lines

We chose a number of ovarian and pancreatic cancer cells lines with variable PARP expression levels to correlate imaging findings and because these primaries are the focus of ongoing clinical trials. UCI 101, UCI 107, OVCA429, and A2780 cell lines were generously provided by Dr Michael Birrer (Massachusetts General Hospital, Boston, MA). All other cell lines were obtained from the ATCC (Manassas, VA). MDA-MB-231, MDA-MB-436, MIA PaCa-2, A2780, OVCAR429, UCI 101, and UCI 107 cells were cultured in RPMI 1640 medium supplemented with 10% fetal bovine serum, L-glutamine, 100 IU penicillin, and 100 μg/ml streptomycin. RAW 264.7, PANC-1, CaOV3, and HT1080 cells were cultured in Dulbecco modified Eagle medium supplemented with 10% fetal bovine serum, 2% sodium bicarbonate, L-glutamine, 100 IU penicillin, and 100 μg/ml streptomycin. SKOV-3 cells were cultured in McCoy 5A medium supplemented with 10% fetal bovine serum, L-glutamine, 100 IU penicillin, and 100 μg/ml streptomycin. OVCAR-3 cells were cultured in RPMI 1640 medium supplemented with 20% fetal bovine serum, 1% bovine insulin, L-glutamine, 100 IU penicillin, and 100 μg/ml streptomycin. OV-90 cells were cultured in 50% MCDB 105 medium, 50% medium 199 supplemented with 15% fetal bovine serum, and 2% sodium bicarbonate. All cell lines were cultured at 37°C and 5% CO_2.

HT1080 H2B-Apple

pmApple-N1 (Myo1E-pmApple-C1; Addgene [Cambridge, MA], Prof. Christien Merrifield [9]) was cloned by ligating mApple into pmCherry-N1 (Clontech, Mountain View, CA) using *Afe*I and *Bsr*G1 restriction enzymes, followed by ligation. The pTag-H2B-Apple construct was produced by subcloning mApple from pmApple-N1 into pTag-H2B-BFP (Evrogen, Moscow, Russia) using the *Age*I and *Not*I

restriction enzyme sites. Correct insertion of mApple was confirmed by sequencing the insert in its entirety. pTag-H2B-Apple was transfected into HT1080 cells using the X-tremeGENE HP transfection reagent (Roche, Basel, Switzerland), followed by selection in 500 μg/ml G418. Single clones were screened for H2B-Apple expression by fluorescence microscopy. Cells were maintained in minimum essential medium supplemented with 10% fetal bovine serum, 100 IU penicillin, 100 μg/ml streptomycin, 2 mM L-glutamine, nonessential amino acids, and 100 μg/ml G418.

In Vitro *Cell Assays*

RAW 264.7, PANC-1, MIA PaCa-2, A2780, OVCAR429, UCI 101, UCI 107, SKOV-3, OVCAR-3, and OV-90 cells (200 μl, 35,000 cells/ml) were each seeded in their respective growth medium on 96-well plates and allowed to attach for 48 hours. After incubation with FL-BO (2 μl, 100 μM, 20 minutes, 37°C), the medium was removed, and the cells were subsequently washed (1× medium, 200 μl, and 2× 1× phosphate-buffered saline [PBS]), fixed (4% paraformaldehyde in PBS), and permeabilized (ice-cold PBS/0.1% Triton X-100/0.5% bovine serum albumin [3× 200 μl, 2× 5-minute and 1× 30-minute incubations]). Cells were then incubated with anti–PARP-1/2 Pab (1:50; Santa Cruz Biotechnology, Santa Cruz, CA) at 4°C overnight, washed with PBS/0.1% Triton X-100 (3× 200 μl), and stained with secondary IgG-Cy5 Pab (1:100; Millipore, Billerica, MA) for 3 hours at 4°C. Before imaging, cells were washed with PBS (1×, 200 μl), stained with both Hoechst 33342 (Invitrogen) and Cellomics blue whole cell stain (Thermo Scientific, Waltham, MA) for 30 minutes at room temperature, and washed again with PBS (3×, 200 μl). Imaging was performed on a DeltaVision microscope (Applied Precision Instruments, Issaquah, WA) at 20×. For each cell line, nine different areas were measured per well. Each cell line was measured in biologic triplicate. FL-BO fluorescence for each cell line was determined by quantifying the total fluorescence and by subtracting the cells' respective green autofluorescence. Relative PARP-1/PARP-2 expression levels were determined by quantifying the fluorescence signal for each cell line and then subtracting unspecific secondary IgG-Cy5 Pab staining.

Mice

Experiments were performed in either C57BL/6 (B6) mice obtained from the Jackson Laboratory (biodistribution, pharmacokinetics; n = 9) or in *nu/nu* mice obtained from Massachusetts General Hospital (tumor implantations, imaging; n = 18). For all surgical procedures and imaging experiments, mice were anesthetized with 2.0% isoflurane in oxygen at 2.0 L/min. For imaging experiments lasting longer than 1 hour, the isoflurane flow rate was reduced to ~1 L/min. Surgeries were conducted under sterile conditions with a zoom stereomicroscope (Olympus SZ61; Olympus America, Center Valley, PA). All procedures and animal protocols were approved by the institutional subcommittee on research animal care.

For window chamber imaging experiments, HT1080 cells (2×10^6 cells, 50 μl 1× PBS) were implanted into dorsal skin chambers (DSCs; APJ Trading Co, Inc, Ventura, CA) in the dorsal skinfold of *nu/nu* mice as described before [10–14]. To allow neovascularization, HT1080 tumors were allowed to grow for 8 days. Spacers between both halves of the DSCs frame prevented excess compression of the tissue and vessels.

To obtain standardized uptake values (SUVs) for ^{18}F-BO, *nu/nu* mice received four subcutaneous injections, each containing SKOV-3, MIA PaCa-2, A2780, or PANC-1 cells, into their flanks and shoulders (2.5×10^6 cells in 100 μl of 70:30 PBS/BD Matrigel [BD Biosciences, Bedford, MA] per injection). Tumors were then allowed to grow for 2 weeks before imaging. For dose-response experiments, *nu/nu* mice each received two subcutaneous injections containing A2780 cells into the flanks (2.5×10^6 cells in 100 μl of 70:30 PBS/BD Matrigel [BD Biosciences] per injection). Tumors were then allowed to grow for 10 to 15 days before the start of imaging experiments.

Intravital Window Chamber Imaging

Mice with HT1080 tumors in their DSCs were injected with 75 nmol of FL-BO (7.5 μl of DMSO, 67.5 μl of *N*,*N*-dimethylacetamide/Solutol (1:1), 150 μl 1× PBS). Accumulation of the probe in HT1080 tumor tissue was imaged *in vivo* in *nu/nu* mice as described previously [11]. A custom-made dorsal skinfold chamber holder was used to stabilize the sample and allow intravital imaging of probe accumulation at single-cell resolution for hours. Static and time series images were collected using a customized Olympus FV1000 based on a BX61-WI confocal microscope (Olympus America). A XLUMPLFLN 20× water immersion objective (NA 1.0) and a 60× LUMFLN (NA 1.10) water immersion objective were used for data collection (both Olympus America). FL-BO and H2B-Apple were scanned and excited sequentially using a 473-nm and a 559-nm diode laser, respectively, in combination with a DM405/488/559/635-nm dichroic beam splitter. Emitted light was then separated and collected using an SDM560 beam splitter and BA490-540 and BA575-675 band-pass filters (all Olympus America). Control tumors were used to optimize imaging conditions by ensuring that no photobleaching or phototoxicity occurred with the imaging settings used.

^{18}F-BO Biodistribution Studies

B6 mice were used for blood half-life determinations. Mice were administered 34 ± 5 μCi of ^{18}F-BO by intravenous tail vein injection. Blood sampling was performed by retro-orbital puncture using tared, heparinized capillary tubes. Samples were subsequently weighed, and activity was measured using an automatic gamma counter (Wallac Wizard 3″ 1480 Automatic Gamma Counter; PerkinElmer, Waltham, MA). Blood half-life data were fitted to a biexponential model (GraphPad Prism 4.0c; GraphPad Software, Inc, San Diego, CA), and results are reported as the weighted average of the distribution and clearance phases. For biodistributions, B6 mice were intravenously injected through the tail vein with either 43 ± 5 μCi (for the 2-hour time point) or 410 ± 22 μCi (for the 18-hour time point) ^{18}F-BO. Animals were then sacrificed at 2 or 18 hours after injection, respectively. Tissues were subsequently harvested and weighed, and their radioactivity was counted using the PerkinElmer Wallac Wizard 3″ 1480 Automatic Gamma Counter. Statistical analysis was performed using GraphPad Prism 4.0c.

PET–Computed Tomography Imaging

Mice were imaged with PET-computed tomography (CT) using an Inveon small animal scanner (Siemens, Munich, Germany). Each PET acquisition took approximately 25 minutes. A high-resolution Fourier rebinning algorithm was used to rebin sinograms, followed by a filtered back-projection algorithm to reconstruct three-dimensional images without attenuation correction. Isotropic image voxel size was 0.796 × 0.861 × 0.861 mm, for a total of 128 × 128 × 159 voxels. Peak sensitivity of the Inveon accounts for 11.1% of positron emission, with a mean resolution of 1.65 mm. More than 100 counts were acquired per pixel, and the mean signal-to-noise ratio was greater than 20. Calibration of the PET signal with a cylindrical phantom containing

^{18}F isotope was performed before all scans. CT images were reconstructed from 360 cone-beam x-ray projections with a power of 80 keV and 500 μA. The isotropic resolution of the CT images was 60 μm. Reconstruction of data sets, PET-CT fusion, and image analysis were done using IRW software (Siemens). Three-dimensional visualizations were produced using the DICOM viewer OsiriX (The OsiriX Foundation, Geneva, Switzerland).

In Vivo *Correlation Experiments*

nu/nu mice bearing A2780 (left shoulder), PANC-1 (right shoulder), MIA PaCa-2 (left flank), and SKOV3 (right flank) tumors were injected with 480 ± 20 μCi of ^{18}F-BO and subjected to PET-CT imaging 2 hours after injection. After imaging, the mice were sacrificed. The tissues were then harvested and weighed, and their radioactivity was counted. After PET and CT image fusion, tumor SUV margins were drawn to span the entire tumor. Drawings were guided with the aid of the CT image using the Siemens Research Workplace v3.0 analysis application.

Western Blot of PARP-1/PARP-2 Expression

After PET imaging and gamma counting, tumors were homogenized in 400 μl of 1× radioimmunoprecipitation assay buffer and 2× Mini Complete Protease Inhibitor Cocktail tablet (Roche, Indianapolis, IN). The samples were spun at 4°C at 10,000 rpm for 10 minutes, and the supernatant was collected. Protein concentration was measured using a bicinchoninic acid protein assay according to the manufacturer's instructions (Thermo Scientific). Tumor lysate (10 μg) was loaded onto NuPAGE Novex 4% to 12% Bis-Tris 1.0-mm gels, and electrophoresis was performed with the XCell SureLock Mini-Electrophoresis system (both Invitrogen). Protein was transferred using the iBlot Dry Blotting System to a nitrocellulose membrane (Invitrogen). The blot was then blocked in 5% nonfat milk for 1 hour, washed with 1× TBS–Tween 20 (Boston BioProducts, Ashland, MA), and incubated overnight at 4°C with 1:1000 anti–PARP-1/2 in 5% nonfat milk (Santa Cruz Biotechnology). After three 5-minute washes and three 30-minute washes with 1× TBS–Tween 20, blots were incubated with 1:5000 goat antirabbit horseradish peroxidase–conjugated secondary antibody (Jackson ImmunoResearch, West Grove, PA) at room temperature for 1 hour. After three 5-minute washes with 1× TBS–Tween 20, blots were incubated with SuperSignal West Pico Chemiluminescent Substrate (Thermo Scientific), exposed for 20 minutes, and then processed with the Kodak (Rochester, NY) X-OMAT 2000A processor. For glyceraldehyde-3-phosphate dehydrogenase (GAPDH) Western blots (after blocking and after three 5-minute washes with 1× TBS–Tween 20), blots were incubated for 1 hour at room temperature with 1:5000 anti–glyceraldehyde-3-phosphate dehydrogenase in 5% nonfat milk (R&D Systems, Minneapolis, MN). After three 5-minute washes with 1× TBS–Tween 20, blots were incubated with donkey antigoat horseradish peroxidase–conjugated secondary antibody (Jackson ImmunoResearch, West Grove, PA) at room temperature for 1 hour. After three 5-minute washes with 1× TBS–Tween 20, blots were incubated with SuperSignal West Pico Chemiluminescent Substrate (Thermo Scientific), exposed for 10 seconds, and then processed with the Kodak X-OMAT 2000A processor.

PET Imaging of Therapeutic Response

nu/nu mice bearing A2780 tumors were injected with 440 ± 40 μCi of ^{18}F-BO through the tail vein and subjected to PET-CT imaging 2 hours after injection. Thereafter, the same mice were reinjected with ^{18}F-FDG (523 ± 47 μCi) and reimaged. After ^{18}F-FDG imaging, the mice were subjected to intraperitoneal injection of 1 mg of Olaparib per mouse formulated in 1:1:4 DMAC/Solutol/PBS (100 μl). The next day, mice were treated with 0.5 mg of Olaparib per mouse. Mice were then imaged as they had been on the first day. This treatment/imaging cycle was repeated for three more days, after which the animals were sacrificed. A total of 10 complete serial sessions were acquired for each mouse. Tumor SUV margins were drawn to span the entire tumor and were accomplished with the aid of the CT images using the Siemens Research Workplace v3.0 analysis application. SUV data from ^{18}F-BO PET images underwent decay correction to the start of ^{18}F-FDG PET imaging and used to correct ^{18}F-FDG SUV data.

Results

Synthesis and Cellular Imaging

Before synthesis, we performed *in silico* modeling to determine which sites of the Olaparib scaffold would tolerate modifications. The docking platform [15] predicted (based on Penning et al. [16]) that the 2*H*-phthalazin-1-one group of ^{18}F-BO would behave in an identical manner to that of Olaparib, namely by binding to the PARP-1–active site (Figures 1*A* and W1*A*). The 4-N*H*-piperazine functionality of Olaparib was shown to tolerate relatively bulky substituents without significantly affecting PARP-1 binding affinity. We thus modified this functionality through an NHS-ester reaction either with BODIPY FL succinimidyl ester to yield FL-BO or with tetrazine succinimidyl ester followed by $^{18/19}$F-*trans*-cyclooctene to yield $^{18/19}$F-BO (Figure 2). The identity and purity of the imaging agents were subsequently confirmed using NMR spectroscopy, HPLC, ESI-MS and high-resolution mass spectrometry. Using a PARP-1 activity assay, we then measured the IC_{50} values for FL-BO (12.2 ± 1.1 nM) and ^{19}F-BO (17.9 ± 1.1 nM), which are similar to the one previously determined for Olaparib (AZD2281, 5 nM [7]) (Figures 1*B* and W1*B*).

Next, we determined the intracellular uptake and localization of FL-BO. Figure 3*A* (Figure W2*A*) shows the typical staining patterns for cell lines incubated with FL-BO, fixed, permeabilized, and then costained with a PARP-1/2 antibody. The drug was found to localize predominantly in the nuclei, particularly in the nucleoli of cells, colocalizing with anti–PARP-1/2. The Pearson correlation coefficient for PANC-1 cells between the PARP antibody stain and FL-BO was $R_{coloc.}$ = 0.95. This correlation was similar for other ovarian and pancreatic cancer cell lines tested. We subsequently investigated whether the total cellular uptake of FL-BO correlated with PARP protein levels. Using different cell lines, we found a good correlation between PARP immunofluorescence and cellular FL-BO accumulation (R^2 = 0.858; Figures 3, *B* and *C*, and W2, *B* and *C*).

Intravital Imaging of FL-BO

We next used a well-established window chamber model to determine the kinetics and cellular distribution of FL-BO at single-cell resolution *in vivo* [11]. Intravenous injection of FL-BO yielded a bright green fluorescent signal, which quickly diffused through the vessels' epithelial cells and resulted in a homogeneous nuclear staining of tumor cells (Figure 4, *top row*). To determine whether cellular accumulation could be inhibited *in vivo*, we also performed competition experiments with nonfluorescent ^{19}F-BO (500 μg injected 90 minutes before

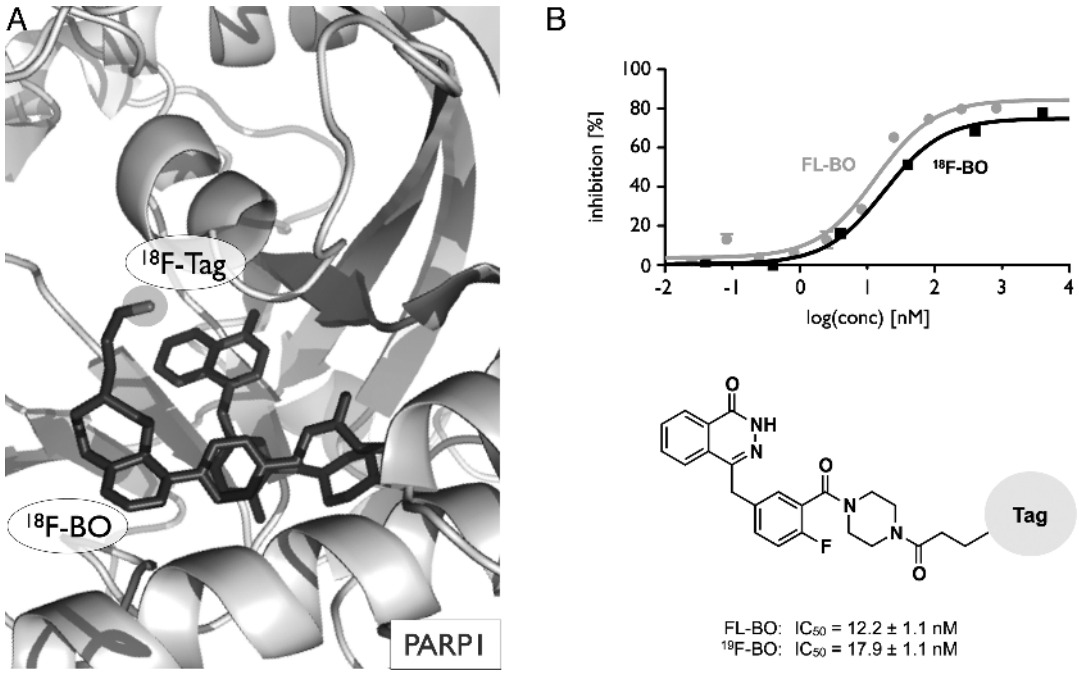

Figure 1. ^{18}F-BO and FL-BO. (A) Binding model depicting ^{18}F-BO and PARP-1, with the 2*H*-phthalazin-1-one binding to the catalytically active site on PARP-1. (B) IC$_{50}$ curves and values for ^{18}F-BO (from Keliher et al. [8]) and FL-BO.

FL-BO). Figure 4 shows that the inhibitor resulted in a marked decrease in uptake of the fluorescent imaging agent (Figure 4, *bottom row*).

Whole-Body Imaging of ^{18}F-BO

The blood half-life for ^{18}F-BO was determined through serial bleeds, and the obtained data points were fitted using a biexponential decay curve. The resulting weighted half-life for ^{18}F-BO was $t_{1/2}$ = 12.4 minutes, with R^2 = 0.828 (Figure 5*A*). Biodistribution studies at 2 hours after injection showed predominant hepatobiliary excretion of ^{18}F-BO (3.9 ± 0.9 and 3.1 ± 1.6%ID/g for liver and small intestines, respectively; Figure 5*C*) with low values in most other host tissues. At 18 hours after injection, the highest amount of probe was found in the feces (Figure 5*D*).

^{18}F-BO was next used to image PARP expression *in vivo*. For this, xenografts of four different human ovarian and pancreatic tumor models (SKOV3, MIA PaCa-2, PANC-1, and A2780, with ascending relative PARP expression profiles) were grown in *nu/nu* mice before tumoral uptake of ^{18}F-BO was determined through PET imaging

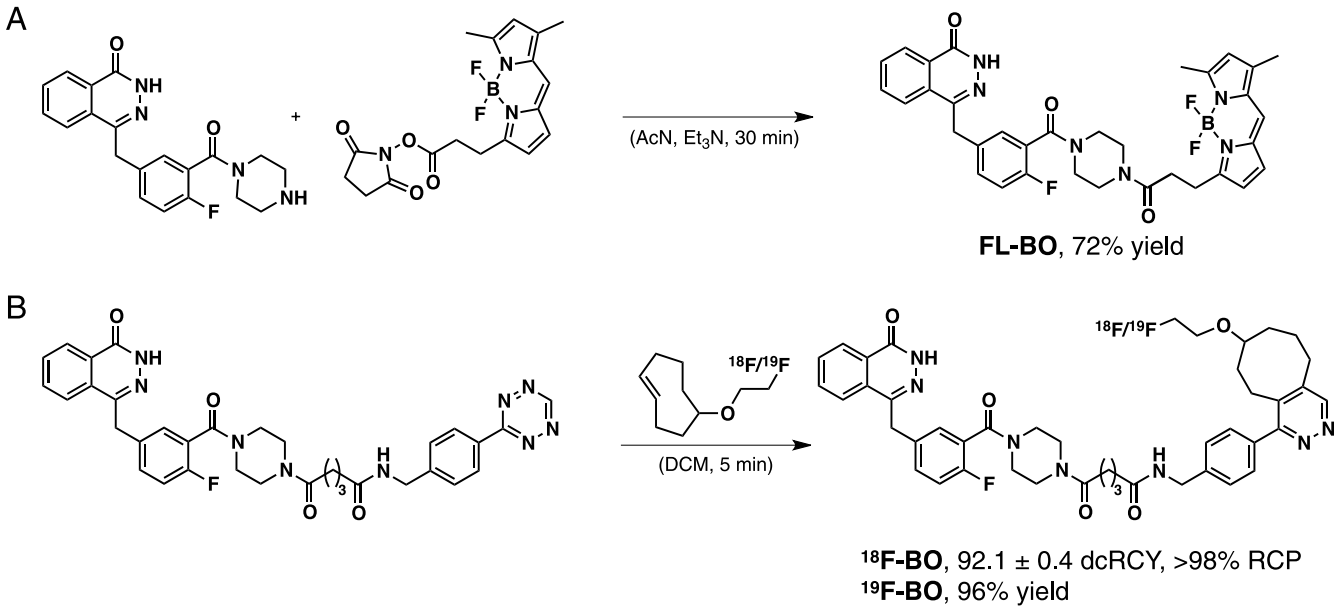

Figure 2. Synthesis of imaging fluorescent and PET active imaging agents. (A) Synthesis of FL-BO: a fluorescent marker for PARP expression *in vitro* and *in vivo*. (B) Synthesis of ^{18}F-BO: a PET agent allowing to measure PARP expression noninvasively *in vivo* [6,8].

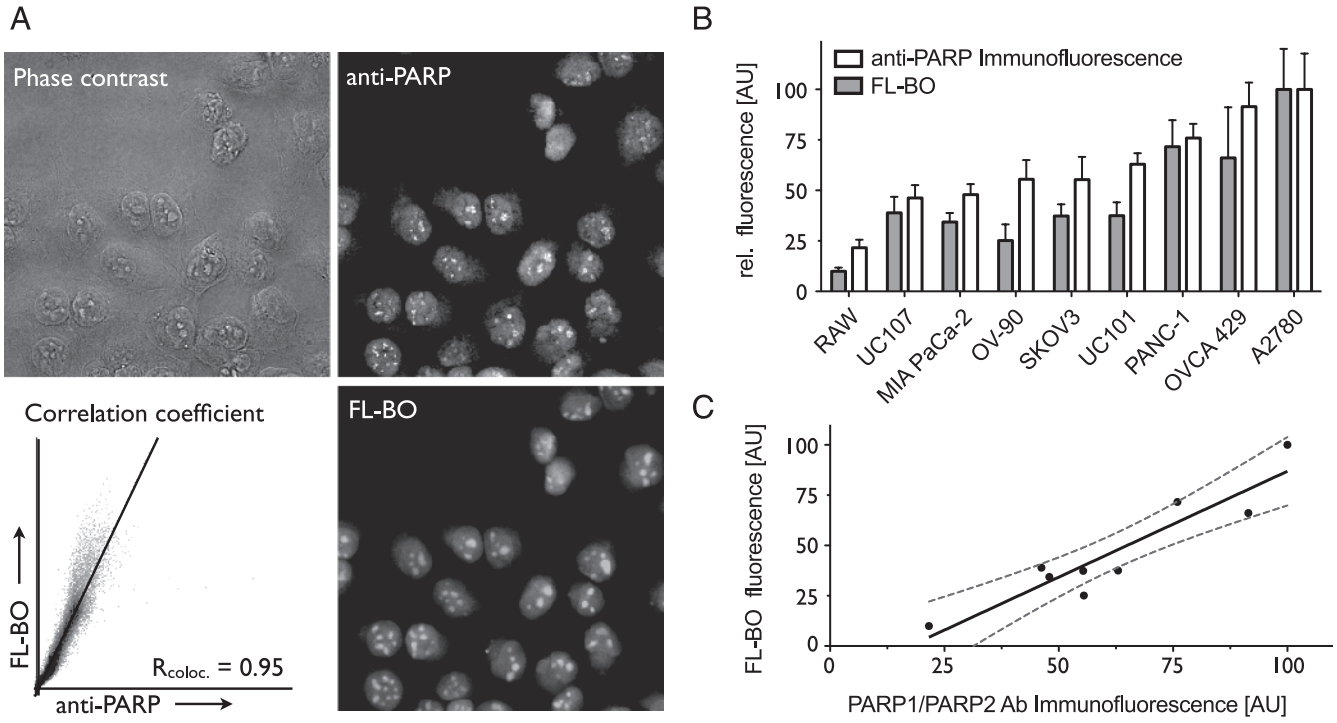

Figure 3. Correlation of cellular FL-BO uptake and relative PARP expression. (A) In PANC-1 cells, there was an excellent correlation between intracellular FL-BO distribution and PARP-1/2 expression: phase contrast (top left), anti-PARP (top right), FL-BO (bottom right), and Pearson correlation coefficient of anti-PARP and FL-BO (bottom left). (B) Column representation of FL-BO uptake and anti-PARP immunofluorescence in different cell lines. (C) Correlation of FL-BO uptake and anti–PARP-1/2 immunofluorescence (dashed line indicates the 95% confidence band).

(Figures 5*B* and W3). The resulting SUVs (Bq/ml) for each of the four tumor types were subsequently quantitated by imaging and then correlated to PARP expression data obtained by Western Blot analysis. Trends for uptake values and Western blot analysis were similar, with A2780 having the highest uptake and expression, followed by PANC-1, MIA PaCa-2, and SKOV3 (Figures 5*B* and W3). Muscle tissue had both the lowest accumulation of ^{18}F-BO and the lowest PARP expression.

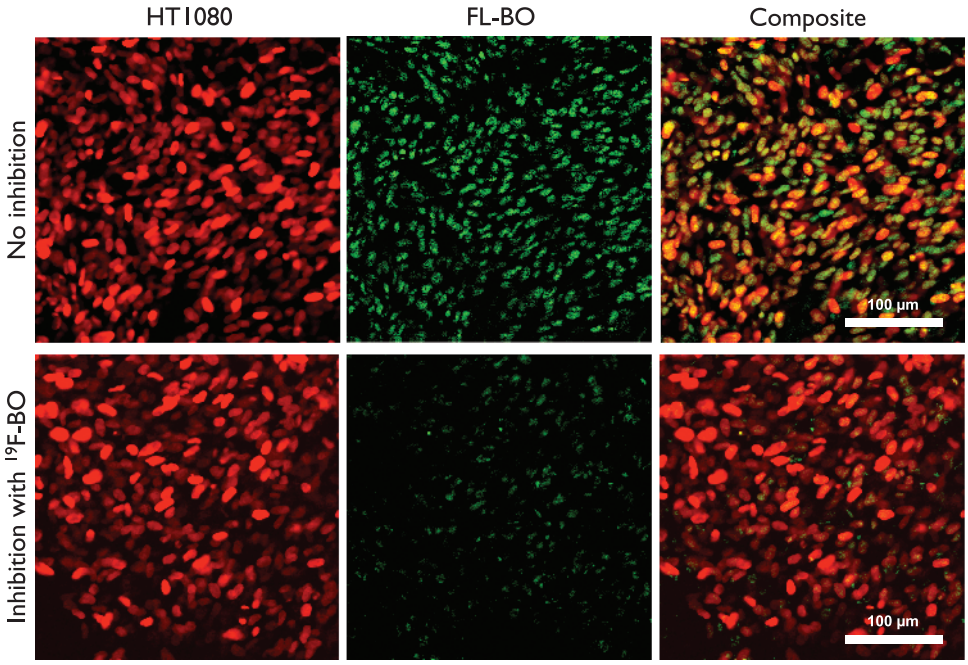

Figure 4. Intravital imaging of FL-BO. Top row (without prior injection of ^{19}F-BO): HT1080 H2B mApple cells (red), FL-BO (green), and composite image. Bottom row (with prior injection of ^{19}F-BO): HT1080 H2B mApple cells (red), FL-BO (green), and composite image. Note the inhibition of FL-BO uptake into tumor cells *in vivo*.

Finally, we determined whether ^{18}F-BO could be used to measure therapeutic drug inhibition *in vivo*. For these experiments, mice bearing A2780 tumor xenografts were serially imaged both before and after Olaparib treatment (Figure 6). Tumoral ^{18}F-BO tumor-muscle ratios were found to be significantly lower ($P < .001$) after single or multiple doses of Olaparib than before treatment in the same animal. As a comparison, we also obtained ^{18}F-FDG scans to determine whether similar effects would be seen. Interestingly, we observed little change in tumor-muscle ratios of ^{18}F-FDG after PARP treatment (Figure 6).

Discussion

Our results show that, in ovarian cancer models, therapeutic doses of Olaparib inhibit PARP *in vivo* and that target inhibition can be quantitated by ^{18}F-BO imaging within hours of initiating treatment. Our experiments were designed to 1) validate ^{18}F-BO for *in vivo* PET imaging, 2) determine the robustness of our new imaging approach in different cancers, 3) directly compare ^{18}F-BO imaging to the clinical standard of ^{18}F-FDG PET imaging (because many cancers use glucose as an energy source [17,18]), and 4) determine the general suitability of the described platform for codeveloping bioorthogonally ^{18}F-labeled companion diagnostics for therapeutic inhibitors. Interestingly, at the early time points investigated, therapeutic PARP inhibition had little effect on the ^{18}F-FDG tumor/muscle imaging signal. In contrast, ^{18}F-BO imaging showed profound changes. These results suggest that ^{18}F-BO imaging could be of value to future clinical trials of PARP inhibitors. Specifically, ^{18}F-BO imaging could be used for dose ranging, testing the comparative efficacy of combination treatments, evaluating treatment efficacy across patient subpopulations, and/or for enrolling (i.e., enriching for) likely responders to PARP inhibitor clinical trials.

PARP inhibitors are a new class of agent that have shown a certain amount of therapeutic efficacy, particularly in BRCA-related malignancies, notably breast and high-grade serous ovarian cancers [4]. For example, a phase 1 clinical study of Olaparib as a monoagent in breast cancer patients with BRCA mutations provided support for the theory of "synthetic lethality" [19]. In a follow-up study, in which the effects of combination therapy were evaluated, resistance to platinum correlated with decreased sensitivity to Olaparib [20]. However, a recent phase 2 clinical trial (ICEBERG 1) [21], using RECIST criteria as the metric of response, failed to show a dose response with Olaparib—suggesting that tumor response to therapy occurs through an alternative mode. In contrast, a more recent report demonstrated that administration of single-agent Olaparib in ovarian cancer patients with BRCA mutations was sufficient to induce tumor responses [5]. It is thus clear that the clinical response to PARP inhibition is varied and that currently accepted markers of such response (progression-free survival, RECIST, PARP inhibition in peripheral blood mononuclear cells, or hair follicles) are insufficiently sensitive (i.e., indirect and/or late). The availability of direct imaging tests capable of measuring PARP inhibition locally would thus be of enormous value in such settings.

The imaging agent used in the present study is based on the Olaparib scaffold with bioorthogonal modifications on the cyclopropane end—a region not essential for target binding [6,22]. Docking simulations showed that ^{18}F-BO, like Olaparib and several other newer PARP inhibitors, binds to the catalytically active region of PARP-1 through its 2*H*-phthalazin-1-one group. The use of bioorthogonal ^{18}F attachment has several advantages over direct fluorination, namely 1) the

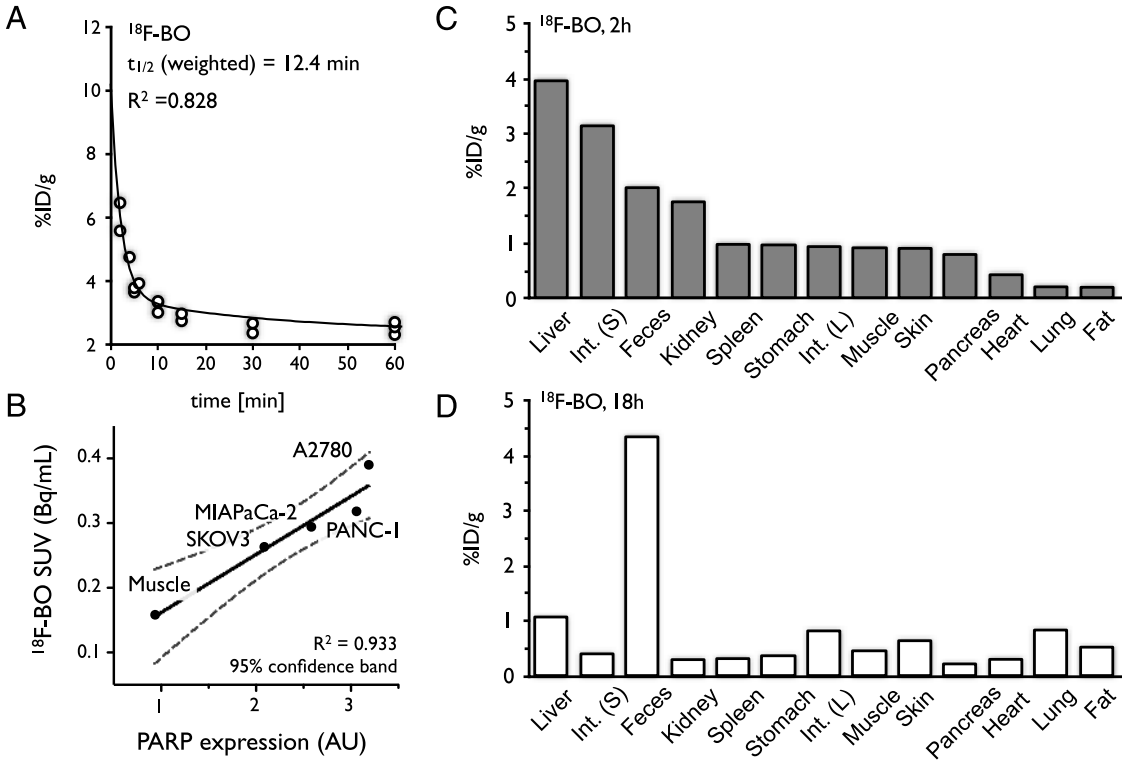

Figure 5. Pharmacokinetics of ^{18}F-BO. (A) Blood half-life of ^{18}F-BO after intravenous administration. (B) Correlation of PARP expression and ^{18}F-BO uptake in four different ovarian and pancreatic tumor types as determined by immunoblot analysis. (C) Biodistribution of ^{18}F-BO at 2 hours after intravenous administration. (D) Biodistribution of ^{18}F-BO at 18 hours after intravenous administration.

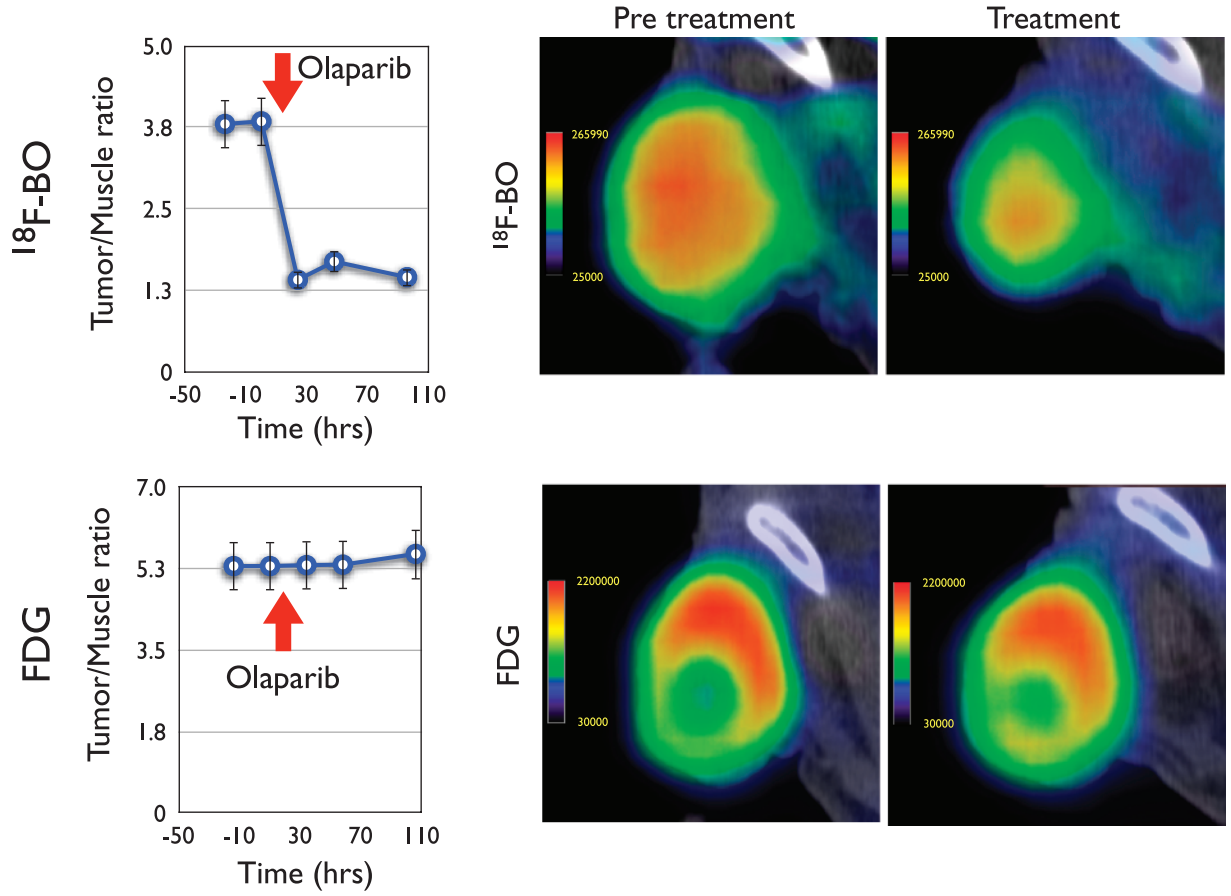

Figure 6. Response of ^{18}F-BO and ^{18}F-FDG uptake to treatment with Olaparib measured in the same mouse. Left: Tumor/muscle plots at different time points before and after initiation of Olaparib treatment. Right: Representative PET-CT images of A2780 tumors (high PARP levels) before and after treatment. Note the changes with ^{18}F-BO and the absence of changes with ^{18}F-FDG. There were no appreciable CT changes in tumor volume during the 24-hour period after Olaparib injection.

rapidity by which imaging agents can be developed, 2) the high synthetic yields, 3) the clean reaction products, 4) the short synthesis times, and 5) the ability to create companion fluorescent agents that can be readily tested through microscopic imaging [23]. Each of these is important in the rapid preparation and validation of companion imaging agents. Although companion imaging agents are structurally similar to their parent inhibitors, they differ importantly in their dosage. Compared with therapeutic doses, diagnostic doses of the imaging agent were approximately 700 times lower for PET imaging and 5 times lower for fluorescence imaging given the different inherent sensitivities of these techniques. In other words, the imaging agent has negligible effects compared with repeatedly administering the therapeutic parent compound.

We used a bioorthogonal approach to tag the small-molecule PARP inhibitor with ^{18}F and convert it into a companion imaging agent. Orthogonal chemistry refers to a highly selective chemical reaction that is both fast and able to take place within living systems. Specifically, we used the *trans*-cyclooctene/tetrazine reaction because it is one of the fastest and most selective chemistries available under physiologic conditions. Additional advantages to this labeling platform include 1) the high translatability of fluorescently and PET-labeled compounds, 2) the standardized synthesis of ^{18}F-labeled bioorthogonal precursors, and 3) the ability to rapidly screen potential targeted molecules of interest. Despite these advances and their benefits, we believe that ^{18}F-BO and other such bioorthogonal small-molecule inhibitors could be improved further. For example, we anticipate the future use of hybrid fluorescent PET/optical tags [24,25]. These would not only enable the rapid translation of fluorescent targeted probes into PET probes but would also allow use of chemically identical molecules with both imaging modalities.

In summary, we describe a generic method for codeveloping bioorthogonally ^{18}F-labeled companion diagnostics for therapeutic inhibitors. Using the example of PARP inhibition, we show that one such agent is able to accurately measure PARP expression levels *in vivo* and thus could be used as a tool to measure therapeutic inhibition within a day of treatment initiation. These agent(s) will likely be of value to the (pre)clinical testing of different PARP inhibitors as well as hopefully other emerging small-molecule inhibitors.

Acknowledgments

The authors thank Joshua Dunham and Jessica Truelove for image processing and generation; Rostic Gorbatov for surgery; Cesar Castro, Matthias Nahrendorf, and Yvonna Fisher-Jeffes for critical review of the article; and Ralph Mazitschek and Sarah Earley for many helpful discussions.

References

[1] Rouleau M, Patel A, Hendzel MJ, Kaufmann SH, and Poirier GG (2010). PARP inhibition: PARP1 and beyond. *Nat Rev Cancer* **10**, 293–301.

[2] Ratnam K and Low JA (2007). Current development of clinical inhibitors of poly(ADP-ribose) polymerase in oncology. *Clin Cancer Res* **13**, 1383–1388.
[3] Comen EA and Robson M (2010). Inhibition of poly(ADP)-ribose polymerase as a therapeutic strategy for breast cancer. *Oncology (Williston Park)* **24**, 55–62.
[4] Gelmon KA, Tischkowitz M, Mackay H, Swenerton K, Robidoux A, Tonkin K, Hirte H, Huntsman D, Clemons M, Gilks B, et al. (2011). Olaparib in patients with recurrent high-grade serous or poorly differentiated ovarian carcinoma or triple-negative breast cancer: a phase 2, multicentre, open-label, non-randomised study. *Lancet Oncol* **12**, 852–861.
[5] Kaye SB, Lubinski J, Matulonis U, Ang JE, Gourley C, Karlan BY, Amnon A, Bell-McGuinn KM, Chen LM, Friedlander M, et al. (2011). Phase II, open-label, randomized, multicenter study comparing the efficacy and safety of Olaparib, a poly (ADP-ribose) polymerase inhibitor, and pegylated liposomal doxorubicin in patients with *BRCA1* or *BRCA2* mutations and recurrent ovarian cancer. *J Clin Oncol* **30**, 372–379.
[6] Reiner T, Keliher EJ, Earley S, Marinelli B, and Weissleder R (2011). Synthesis and *in vivo* imaging of a ^{18}F-labeled PARP1 inhibitor using a chemically orthogonal scavenger-assisted high-performance method. *Angew Chem Int Ed Engl* **50**, 1922–1925.
[7] Menear KA, Adcock C, Boulter R, Cockcroft XL, Copsey L, Cranston A, Dillon KJ, Drzewiecki J, Garman S, Gomez S, et al. (2008). 4-[3-(4-Cyclopropanecarbonylpiperazine-1-carbonyl)-4-fluorobenzyl]-2*H*-phth alazin-1-one: a novel bioavailable inhibitor of poly(ADP-ribose) polymerase-1. *J Med Chem* **51**, 6581–6591.
[8] Keliher EJ, Reiner T, Turetsky A, Hilderbrand SA, and Weissleder R (2011). High-yielding, two-step ^{18}F labeling strategy for ^{18}F-PARP1 inhibitors. *ChemMedChem* **6**, 424–427.
[9] Taylor MJ, Perrais D, and Merrifield CJ (2011). A high precision survey of the molecular dynamics of mammalian clathrin-mediated endocytosis. *PLoS Biol* **9**, e1000604.
[10] Falkvoll KH, Rofstad EK, Brustad T, and Marton P (1984). A transparent chamber for the dorsal skin fold of athymic mice. *Exp Cell Biol* **52**, 260–268.
[11] Orth JD, Kohler RH, Foijer F, Sorger PK, Weissleder R, and Mitchison TJ (2011). Analysis of mitosis and antimitotic drug responses in tumors by *in vivo* microscopy and single-cell pharmacodynamics. *Cancer Res* **71**, 4608–4616.
[12] Lehr HA, Leunig M, Menger MD, Nolte D, and Messmer K (1993). Dorsal skinfold chamber technique for intravital microscopy in nude mice. *Am J Pathol* **143**, 1055–1062.
[13] Makale M (2007). Intravital imaging and cell invasion. *Methods Enzymol* **426**, 375–401.
[14] Alexander S, Koehl GE, Hirschberg M, Geissler EK, and Friedl P (2008). Dynamic imaging of cancer growth and invasion: a modified skin-fold chamber model. *Histochem Cell Biol* **130**, 1147–1154.
[15] Trott O and Olson AJ (2010). AutoDock Vina: improving the speed and accuracy of docking with a new scoring function, efficient optimization, and multithreading. *J Comput Chem* **31**, 455–461.
[16] Penning TD, Zhu GD, Gong J, Thomas S, Gandhi VB, Liu X, Shi Y, Klinghofer V, Johnson EF, Park CH, et al. (2010). Optimization of phenyl-substituted benzimidazole carboxamide poly(ADP-ribose) polymerase inhibitors: identification of (*S*)-2-(2-fluoro-4-(pyrrolidin-2-yl)phenyl)-1*H*-benzimidazole-4-carboxamide (A-966492), a highly potent and efficacious inhibitor. *J Med Chem* **53**, 3142–3153.
[17] Locasale JW, Cantley LC, and Vander Heiden MG (2009). Cancer's insatiable appetite. *Nat Biotechnol* **27**, 916–917.
[18] Vander Heiden MG, Cantley LC, and Thompson CB (2009). Understanding the Warburg effect: the metabolic requirements of cell proliferation. *Science* **324**, 1029–1033.
[19] Fong PC, Boss DS, Yap TA, Tutt A, Wu P, Mergui-Roelvink M, Mortimer P, Swaisland H, Lau A, O'Connor MJ, et al. (2009). Inhibition of poly(ADP-ribose) polymerase in tumors from *BRCA* mutation carriers. *N Engl J Med* **361**, 123–134.
[20] Fong PC, Yap TA, Boss DS, Carden CP, Mergui-Roelvink M, Gourley C, De Greve J, Lubinski J, Shanley S, Messiou C, et al. (2010). Poly(ADP)-ribose polymerase inhibition: frequent durable responses in *BRCA* carrier ovarian cancer correlating with platinum-free interval. *J Clin Oncol* **28**, 2512–2519.
[21] Audeh MW, Carmichael J, Penson RT, Friedlander M, Powell B, Bell-McGuinn KM, Scott C, Weitzel JN, Oaknin A, Loman N, et al. (2010). Oral poly(ADP-ribose) polymerase inhibitor Olaparib in patients with *BRCA1* or *BRCA2* mutations and recurrent ovarian cancer: a proof-of-concept trial. *Lancet* **376**, 245–251.
[22] Reiner T, Earley S, Turetsky A, and Weissleder R (2010). Bioorthogonal small-molecule ligands for PARP1 imaging in living cells. *Chembiochem* **11**, 2374–2377.
[23] Pittet MJ and Weissleder R (2011). Intravital imaging. *Cell* **147**, 983–991.
[24] Hendricks JA, Keliher EJ, Wan D, Hilderbrand S, Weissleder R, and Mazitschek R (in press). Synthesis of ^{18}F-BODIPY as bifunctional reporter for hybrid optical/PET imaging. *Angew Chem Int Ed Engl*. doi: 10.1002/anie.201107957.
[25] Li Z, Lin TP, Liu S, Huang CW, Hudnall TW, Gabbai FP, and Conti PS (2011). Rapid aqueous [^{18}F]-labeling of a BODIPY dye for positron emission tomography/fluorescence dual modality imaging. *Chem Commun (Camb)* **47**, 9324–9326.

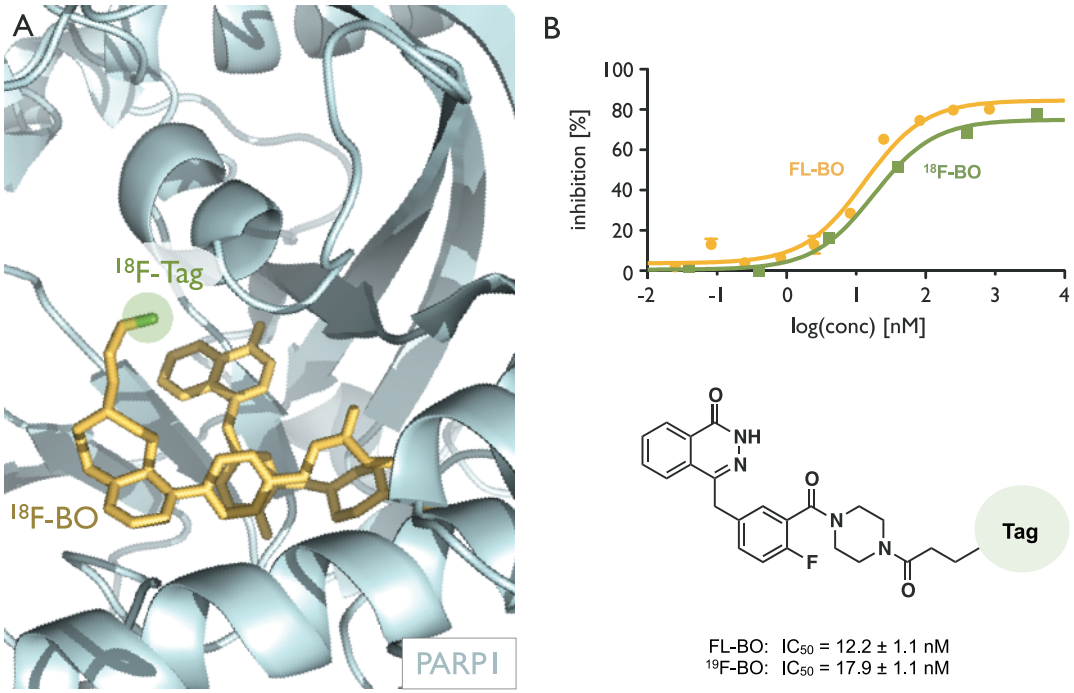

Figure W1. ^{18}F-BO and FL-BO. (A) Binding model depicting ^{18}F-BO and PARP-1, with the 2*H*-phthalazin-1-one binding to the catalytically active site on PARP-1. (B) IC_{50} curves and values for ^{18}F-BO and FL-BO (from Keliher et al. [8]).

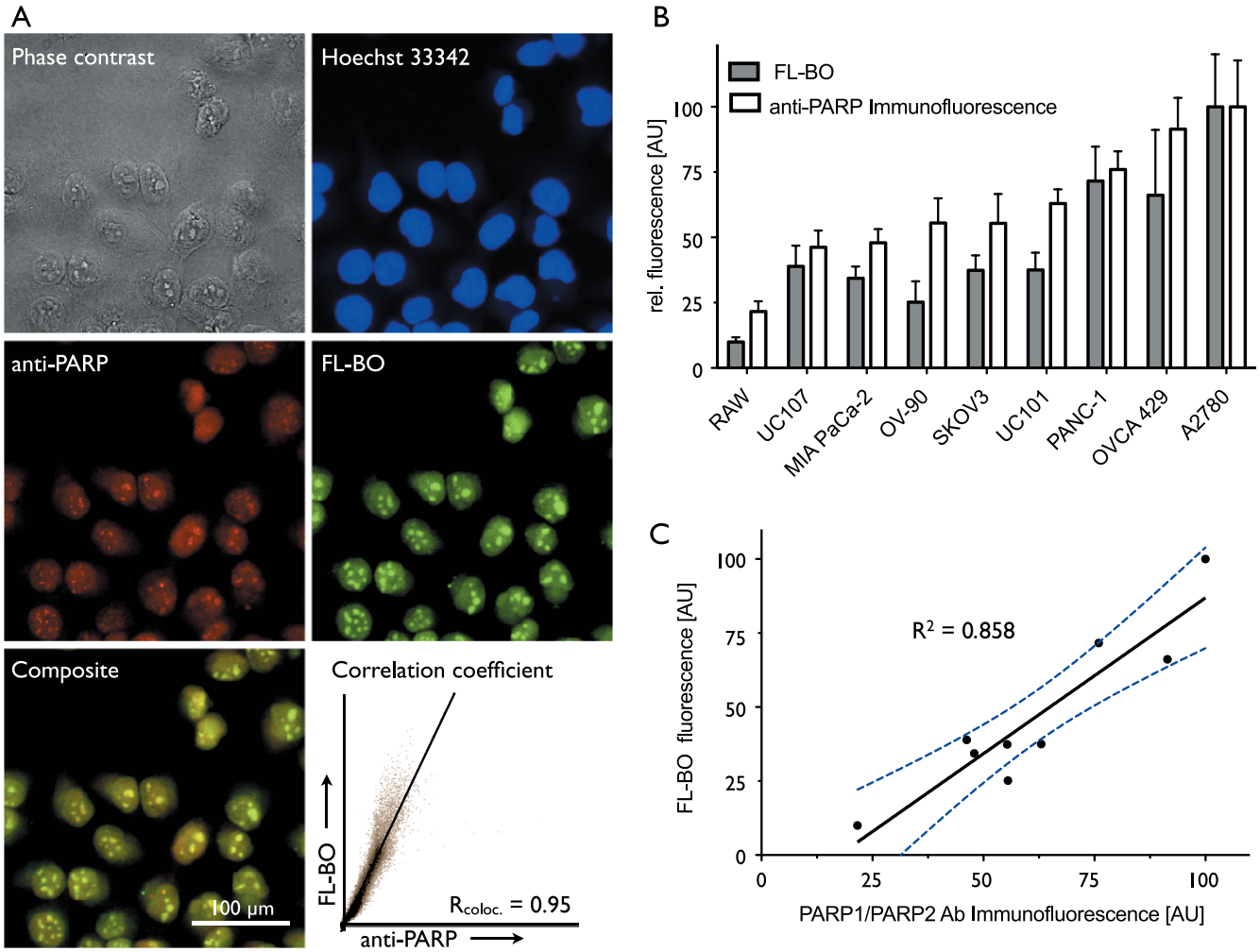

Figure W2. Correlation of cellular FL-BO uptake and relative PARP expression. (A) In PANC-1 cells, there was an excellent correlation between intracellular FL-BO distribution and PARP-1/2 expression: phase contrast (grayscale), Hoechst 33342 (blue), anti-PARP (red), FL-BO (green), composite image of anti-PARP and FL-BO, and Pearson correlation coefficient of anti-PARP and FL-BO. (B) Column representation of FL-BO uptake and anti-PARP immunofluorescence in different cell lines. (C) Correlation of FL-BO uptake and anti–PARP-1/2 immunofluorescence (blue line indicates the 95% confidence band).

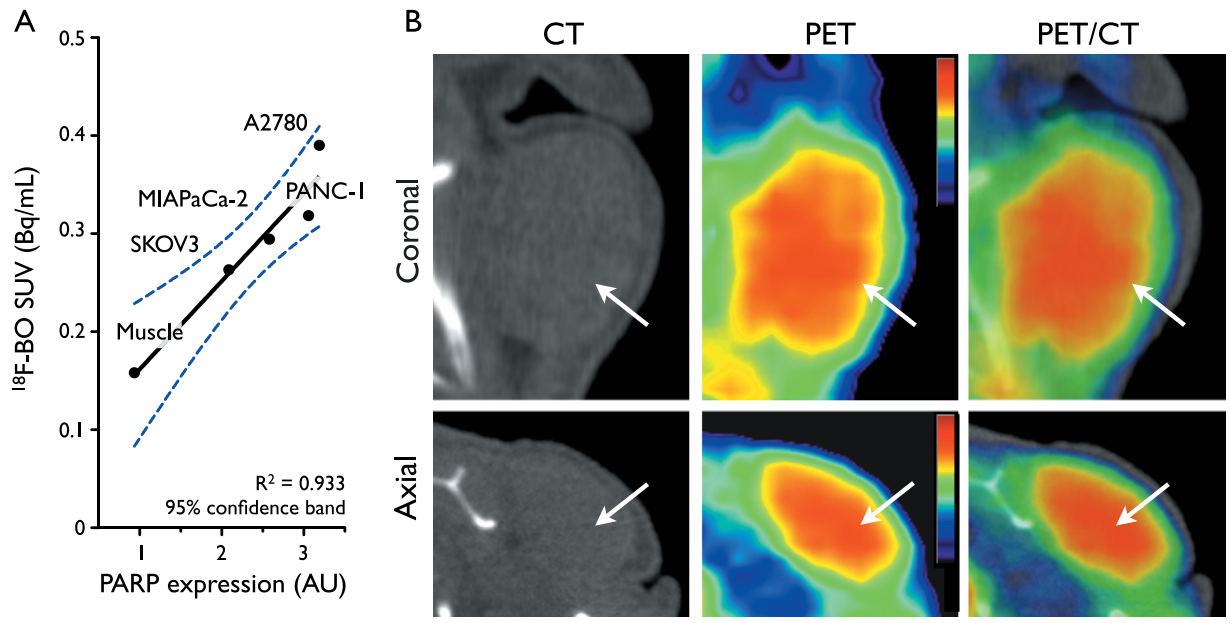

Figure W3. Correlation of PARP expression and ^{18}F-BO uptake in tumor tissue. (A) correlation of uptake and PARP expression in four different ovarian and pancreatic tumor types as determined by immunoblotting. (B) coronal and axial CT and PET scans of a representative A2780 tumor implanted in the shoulder of a mouse.